COMPUTER PROCESSING AND MODELING – Review Article

Magnetic Resonance in Medicine 65:1470–1482 (2011)

Calculation of Radiofrequency Electromagnetic Fields and Their Effects in MRI of Human Subjects

Christopher M. Collins[1]* and Zhangwei Wang[2]

Radiofrequency magnetic fields are critical to nuclear excitation and signal reception in magnetic resonance imaging. The interactions between these fields and human tissues in anatomical geometries results in a variety of effects regarding image integrity and safety of the human subject. In recent decades, numerical methods of calculation have been used increasingly to understand the effects of these interactions and aid in engineering better, faster, and safer equipment and methods. As magnetic resonance imaging techniques and technology have evolved through the years, so to have the requirements for meaningful interpretation of calculation results. Here, we review the basic physics of radiofrequency electromagnetics in magnetic resonance imaging and discuss a variety of ways radiofrequency field calculations are used in magnetic resonance imaging in engineering and safety assurance from simple systems and sequences through advanced methods of development for the future. Magn Reson Med 65:1470–1482, 2011. © 2011 Wiley-Liss, Inc.

Key words: MRI; electromagnetics; radiofrequency; signal; noise; SAR; safety

Only 10 years ago, the task of reviewing the literature on radiofrequency (RF) field calculations performed with an attempt to consider the human subject in magnetic resonance imaging (MRI) would be a seemingly manageable task, and could even be comprehensive without being prohibitively long. The combination of increasing reliance on numerical calculations and increasing complexity of RF techniques and technology in MRI makes this much more challenging today. In this work, the fundamental roles of the RF fields in MRI are discussed before a basic example calculation of signal-to-noise ratio (SNR) and specific energy absorption rate (SAR) for a particular imaging sequence in a sphere of biological tissue is presented using analytical methods. Following a brief transition, an attempt to review the literature on current applications with emphasis on breadth more than depth is given. It is hoped that the end result will provide enough basic understanding to the reader that with further study of the references provided he or she may be comfortable pursuing calculations for new purposes, continuing to advance the frontiers of MRI.

RF MAGNETIC FIELDS FOR MRI: NUCLEAR EXCITATION AND SIGNAL RECEPTION

In MRI, a variety of magnetic fields is applied to the human body to manipulate the magnetic moments of nuclei in the tissue so that they produce a detectable RF signal. An equation often used to describe the behavior of the net nuclear magnetization vector (**M**) in the presence of a general applied magnetic field (**B**) at a single location is the Bloch equation, sometimes written as

$$\frac{d\mathbf{M}}{dt} = \gamma(\mathbf{M} \times \mathbf{B}) - \left(\frac{M_x}{T_2}\mathbf{a}_i + \frac{M_y}{T_2}\mathbf{a}_j + \frac{M_z - M_0}{T_1}\mathbf{a}_k\right) \quad [1]$$

where γ is the gyromagnetic ratio, T_1 and T_2 are the longitudinal and transverse relaxation rates, respectively, M_0 is the magnitude of the net nuclear magnetization at rest, proportional to the strength of a given z-oriented static magnetic field (B_0), and $\mathbf{a}_i$, $\mathbf{a}_j$, and $\mathbf{a}_k$ are unit vectors in the x, y, and z directions. The first term on the right-hand-side (including the cross product) indicates that when no other fields are applied ($\mathbf{B} = B_0\mathbf{a}_z$) any transverse ($x$- and/or y-oriented) components of **M** will precess about the z-axis (the direction of B_0) at a rate proportional to γ. This precession of the nuclei from a classical point of view is very much analogous to the precessional motion of a spinning gyroscope "on its side" in a gravitational field, and, thus, the transverse component of the net nuclear magnetization vector can be seen to rotate in a plane perpendicular to B_0, and will have the potential to induce a detectable RF current in nearby conductors. Figure 1 illustrates the net magnetization vector from an ensemble of precessing nuclei, the transverse component of which (M_T) will induce a current in the coil and detectable signal voltage (V_S) at the coil terminals. The effect of the remaining terms in the right-hand side indicate that the signal-inducing transverse components of the magnetization vector will decay to zero, whereas the longitudinal component M_z will approach M_0. When the sample has been in the presence of B_0 alone for an appreciable length of time, typically more than a few seconds, no RF signal is available. It is then necessary to excite the nucluei.

From a classical perspective, nuclear excitation can also be understood by considering the precession-related portion of Eq. 1 in a frame of reference that rotates at the same speed as nuclear precession about B_0. Here, a circularly polarized component (B_1^+) of an applied RF magnetic field $\mathbf{B}_1$ that rotates at the rate of nuclear precession will appear as a static magnetic field, and the nuclear magnetization vector will precess about B_1^+.

[1]Department of Radiology, The Pennsylvania State University, Hershey, Pennsylvania, USA.

[2]GE Healthcare, Aurora, Ohio, USA.

Grant numbers: NIH R01 EB000454 and NIH R01 EB006563.

*Correspondence to: Christopher M. Collins, Ph.D., NMR/MRI Building, H066, 500 University Dr., Hershey, PA 17033, USA.
E-mail: ccollins@hmc.psu.edu

Received 17 June 2010; revised 23 November 2010; accepted 5 January 2011.

DOI 10.1002/mrm.22845
Published online 4 March 2011 in Wiley Online Library (wileyonlinelibrary.com).

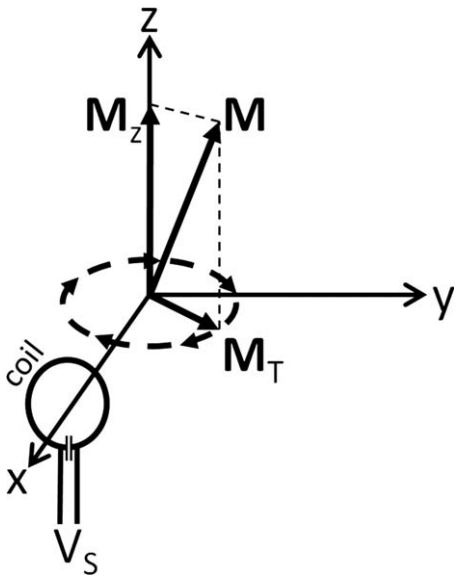

FIG. 1. The transverse component (M_T) of the net nuclear magnetization (M) precessing in a z-oriented static magnetic field can induce a detectable voltage (V_S) in a nearby conductive coil.

In this work, B_1^+ is a complex quantity. It is important to note that in MRI, complex numbers are often used either to describe magnitude and phase of a quantity varying sinusoidally with time (as using phasor notation common in many fields of study) or to describe magnitude and orientation in a rotating frame for a circularly polarized component of a time-varying vector quantity. The two are related, e.g., the phase of the voltage transmitted to an RF coil determines the orientation of the resulting B_1^+ in the rotating frame, but there are also important differences and it is very important to maintain clarity on the meaning of complex numbers in each instance. For example, it should be clear that for a continuous wave excitation, both the magnitude of B_1^+ and its orientation in the rotating frame are constant through time (assuming, of course, that the rotating frame used is rotating with nuclear precession at a frequency equal to the applied RF field). A thorough discussion of the relationship in MRI between these two different meanings for complex numbers is given by Hoult (1). In this work, complex numbers indicate magnitude and orientation in the rotating frame for B_1^+, B_1^-, B_1^{cc}, B_1^{cw}, and M_T. In several other quantities (M_x, M_y, B_x, B_y, E_x, E_y, E_z, E_ϕ), complex numbers are used to indicate magnitude and phase using phasor notation.

Figure 2 shows a circularly polarized component of an RF field B_1^+ inducing precession in the rotating frame. In reality, the frequency of nuclear precession may be slightly different from that of the applied RF field due to local inhomogeneities in the B_0 field, applied gradient fields, or frequency-specific elements in the RF pulse design. An expression for **B** in the rotating frame that accounts for all these elements might take the form

$$\mathbf{B}(r,t) = \mathrm{Re}\{\mathrm{B}_1^+(r,t)\}\mathbf{a}_i + \mathrm{Im}\{\mathrm{B}_1^+(r,t)\}\mathbf{a}_j + \left(\frac{\Delta\omega(r,t)}{\gamma}\right)\mathbf{a}_k + G(r,t)\mathbf{a}_k \quad [2]$$

where r indicates position, the $\Delta\omega$ is used to account for B_0 inhomogeneity, chemical shift, and/or design-related offset between the applied RF frequency and the frequency of nuclear precession, and G is the local field resulting from application of the gradients.

Most commonly, MRI requires 1) a static magnetic field, B_0, by convention oriented either parallel or antiparallel to the z direction, 2) application of "transmit" RF magnetic fields, B_{1t}, to excite the nuclei and create a sizeable transverse component to M, 3) switched magnetic field gradients in three orthogonal directions, G_x, G_y, and G_z, to achieve spatially selective excitation and encode spatial information into the frequency and phase of the received signal, and 4) passive conductors or "receive coils" near the sample to detect the signal. By reciprocity, the strength of the signal induced in a given receive coil will be proportional to a circularly polarized component of the magnetic field that rotates in the direction opposite nuclear precession, B_{1r}^-, produced by the receive coil when driven at the frequency of interest. The necessity of considering the counter-rotating component during reception has been demonstrated and discussed in a variety of ways (1–3). An easy way to illustrate the need is by considering a case where a coil used in excitation and reception is located along the z-axis at some location from a small sample, also located along the z-axis. Figure 3 illustrates this case. Using the right-hand rule with the thumb indicating the direction of travel, a circularly-polarized field traveling from the coil to the sample will have the opposite sense of rotation than a circularly polarized field traveling from the sample to the coil if the direction of rotation matches that of nuclear precession in the sample—as it clearly should in each case.

For purposes of simulation, the demodulated instantaneous signal induced in a single receive coil can be expressed (1)

$$S = 2\omega \int M_T B_1^{-*} \mathrm{d}V \quad [3]$$

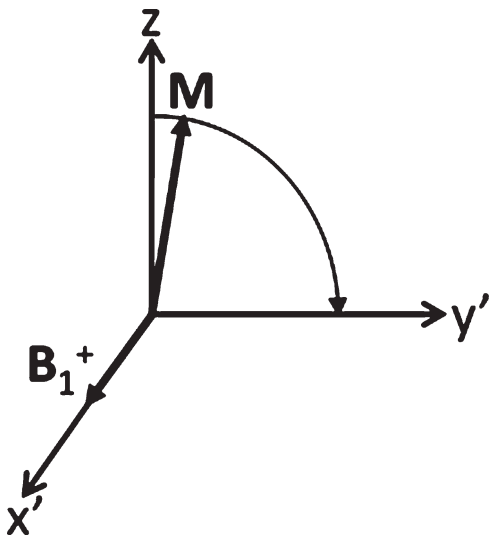

FIG. 2. A circularly polarized component of an RF magnetic field with frequency and direction of rotation matching those of nuclear precession (B_1^+) will induce a second precession of the net nuclear magnetization vector in a rotating frame of reference also with frequency and direction of rotation matching those of nuclear precession.

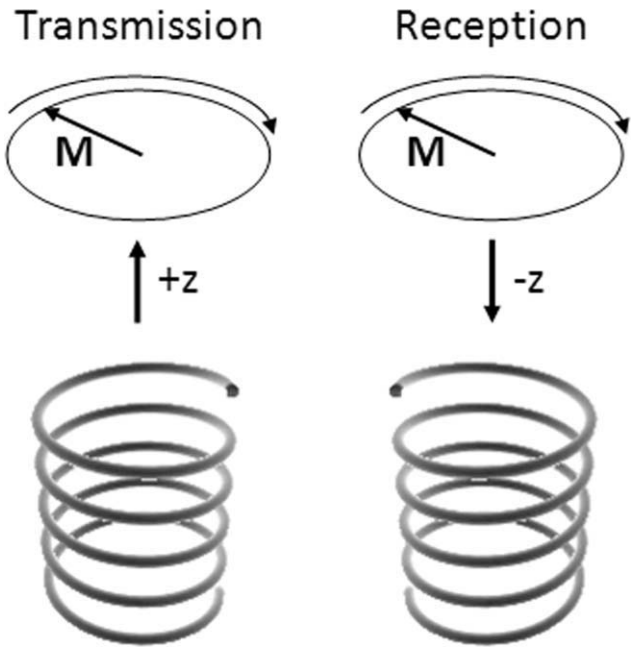

FIG. 3. Illustration of the need to consider oppositely rotating RF field components in transmission and reception. Considering a hypothetical arrangement where circularly polarized traveling waves are used to interact with the nuclei, even though the direction of nuclear precession is constant, due to the different direction of travel of the fields in transmission and reception, the pertinent field has an opposite sense of rotation with respect to the direction of travel. In the hypothetical case that helical antennas designed to produce circularly polarized fields are used, antennas with different "handedness" will be required in transmission and reception. Similarly, consideration of oppositely rotating components of a coil capable of producing both components will be required in calculating transmit and receive distributions for that coil. (Note that design considerations for a helical antenna to operate predominantly in end-fire mode and to produce a circularly polarized wave are specific and require—among other things—that the circumference of the antenna be close to one wavelength. Also, the effects of the magnet bore and human subject on actual wave polarization would require further study, and thus, this reference to the hypothetical helical antenna is only for illustrative purposes at this time.)

where S has units of volts and is complex, with its complex nature being related to magnitude and phase using phasor notation, and ω is the frequency of nuclear precession. In an experiment, the phase of the signal will depend on a number of additional parameters including coil electrical properties and where along the receive chain the signal is measured. For S to correspond to experimental values, B_1^- should be calculated with unit current in the coil (4).

Between Eqs. 2 and 3, it is clear that circularly polarized components of RF magnetic fields are necessary for MRI in both excitation and reception of signal. In general, the circularly polarized components of an RF magnetic field can be calculated as

$$B_1^{cc} = (B_x + iB_y)/2 \quad [4a]$$

$$B_1^{cw} = (B_x^* + iB_y^*)/2 \quad [4b]$$

Whether the clockwise-rotating component (B_1^{cw}) or counter-clockwise rotating component (B_1^{cc}) of the B_1 field rotates in the same direction as nuclear precession (giving B_1^+ for the transmit coil) is determined by the orientation of B_0 (with or against the z-axis); the remaining component, rotating opposite nuclear precession, gives B_1^- for the receive coil or coils. By convention, nuclear precession is left handed with respect to B_0 (or clockwise with B_0 in the positive z-direction) (5). Importantly, when calculating B_1^- for a quadrature coil in reception, it is necessary to drive the coil with all sources having opposite phases to those used in transmission. This can be thought of as driving the coil through the receive channel of the quadrature splitter/combiner.

RF ELECTRIC FIELDS IN MRI: TISSUE HEATING (SAR) AND SAMPLE NOISE

Typically, B_0 fields with strengths on the order of Tesla (T) are used to image signal from the hydrogen (^{1}H) nucleus, which has a γ of 42.58 MHz/T. Today, B_0 field strengths of up to 7 T are used in whole-body human MRI and up to 9.4 T are used in head-only MRI, requiring RF fields and resulting in RF signals at up to 300 MHz in whole-body MRI and up to 400 MHz in head-only MRI, and the trend toward higher field strengths continues with an 11.7 T (500 MHz) whole-body human system under development for Saclay, France in 2012. Although they have no positive effects in MRI, as we know from the Maxwell equations, electric fields are naturally induced by a time-varying magnetic field (as seen in Faraday's Law, given as Eq. 8 later in this work), and also can arise from the distribution of electrical potential on nearby wires (as seen in Gauss's Law, $\nabla \cdot E = \rho/\varepsilon_0$, where E is electric field, ρ is charge density, and ε_0 is electric permittivity of free space). In MRI, the electric fields from these two sources are sometimes called "magnetically induced" and "conservative" (6) or alternately "inductive" and "capacitive" (4). For regions of interest, coil sizes, and frequencies most often used in human MRI today the magnetically induced fields are generally expected to be dominant with the conservative portion being negligible, but in some situations, the effect of the conservative fields can be greater than those of the magnetically induced. However, the conservative electric fields should be kept in mind especially for cases with small coils and/or low frequencies compared to those common in MRI today, or if capacitive gaps are extremely close to the sample. For the remainder of this work they are assumed to be negligible.

Electrical fields produced in the conductive tissues during transmission of B_1 fields during nuclear excitation will drive electrical currents in the tissue and result in tissue heating. This heating can be significant and is regulated to avoid adverse effects (7). The quantity most directly monitored in MRI today is the whole-body specific energy absorption rate (SAR, W/kg), or the amount of energy absorbed over the whole body over any 6 min period of time divided by the mass of the body. This is estimated a variety of ways in practice, but in principle is equal to the time-average power absorbed by the whole body divided by the mass of the body, and thus has units of W/kg. There are additional regulations

on the SAR over the head, any portion of the body, and any 10 g region of the body (7). All these quantities are also estimated in a variety of ways in practice, and numerical field calculations are used increasingly in their estimation, as will be discussed later in this work. With knowledge (or estimates) of the electrical fields throughout the tissue, SAR over a volume of interest can be calculated as

$$\mathrm{SAR} = \int \frac{\sigma\left(|E_x|^2+|E_y|^2+|E_z|^2\right)}{2\rho}\mathrm{d}V \qquad [5]$$

where σ is material conductivity, ρ is material mass density, and E_x, E_y, and E_z are the amplitudes of orthogonal components of the electric field.

Tissue conductivity arises from (among other things) translation of ions and rotation of dipoles under the influence of an applied electric field (8). Although no RF electric fields are applied during signal reception in MRI, by the principle of reciprocity the magnitude of the RF electrical field associated with the receive coil at a given location is proportional to the sensitivity of the coil to (among other things) random translation of ions and rotation of dipoles in the tissue. Thus, it is by a reciprocal argument that we can calculate the noise induced in the coil as being proportional to both the electric field strength of the receive coil and the square root of the sample conductivity, and thus proportional to the square root of power dissipated in the tissue when the receive coil is driven. Random thermal noise is induced by the conductive portions of the entire sample volume at all times, and its root mean square amplitude can be calculated as

$$N = \sqrt{4kTP_{\mathrm{diss}}\mathrm{BW}} \qquad [6]$$

where k is the Boltzmann constant, T is absolute temperature, P_{diss} is power dissipated in the sample when the receive coil is driven with 1 A, and BW is the bandwidth of the digital filters used to filter out noise not within the bandwidth of the signal. Although it is necessary to calculate P_{diss} or B_1^- with 1 A in the receive coil to get meaningful values for either S or N alone, to get meaningful calculations of signal-to-noise ratio (SNR), it is only necessary that P_{diss} be calculated under the same conditions (driving voltage or coil current, etc.) as for the calculation of B_1^- in the signal calculation. In some cases (especially for relatively small receive coils and/or low frequencies), noise from the coil can also be significant. In these cases, an equation much like Eq. 6 can be used to calculate coil noise as well

$$N = \sqrt{4k(T_{\mathrm{sample}}P_{\mathrm{sample}}+T_{\mathrm{coil}}P_{\mathrm{coil}})\mathrm{BW}} \qquad [7]$$

Occasionally, a term for radiated power is also seen in the representation for noise. This can be convenient when using calculations or measurements representing power dissipated in a limited space (9), but because MRI of humans typically occurs in a room with a closed RF screen, it is expected that all RF power that might otherwise be "radiated" will be dissipated somewhere in the room, almost entirely in lossy dielectric material such as the human body. At frequencies below about 300 MHz, very little RF energy will even escape the magnet bore (9,10).

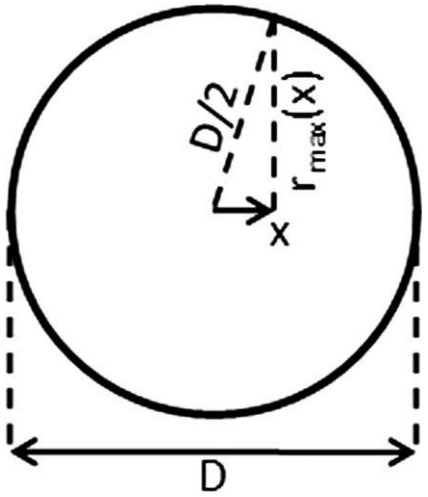

FIG. 4. Geometrical considerations for illustrative calculation of power absorbed by a sphere of conductive material in a perfectly homogeneous linearly polarized RF magnetic field.

SIMPLE, LOW-FREQUENCY, ANALYTICAL EXAMPLE

Much of this article is dedicated to brief descriptions of and references to advanced methods with complex results such that they cannot be fully contained or described herein. Before beginning that portion of the review, however, it may be useful to consider a simple example in some detail. This will provide a tangible illustration as well as a reference point for more advanced cases.

Consider a hypothetical situation where a perfectly homogeneous linearly polarized RF magnetic field with an amplitude of 4μT is induced in a head-sized (15-cm diameter) sphere with electrical properties of human brain (σ = 0.4 S/m, ε_r = 116) at 42.6MHz (B_0 = 1T) when an RF coil is driven with 1 A. Assume that at this frequency, one wavelength in the sample is long enough compared to the sample diameter that we can estimate the electric field strengths induced in the sphere using a quasi-static approximation by applying only Faraday's Law

$$\oint \mathbf{E}\cdot\mathrm{d}l = -i\omega\iint \mathbf{B}\cdot\mathrm{d}s \qquad [8]$$

If the applied linearly polarized field is oriented with the x-axis, due to symmetry we can use Eq. 8 to show that the magnitude of the electric field E in the sphere at any radius r from any location on the x-oriented axis through the center of the sphere is equal to $\omega rB/2$. With reference to Fig. 4 and using some simple trigonometric relations, it is possible to show that the maximum value for r within the sphere at any value for x is equal to

$$r_{\max} = \frac{D}{2}\sqrt{1-\frac{4x^2}{D^2}} \qquad [9]$$

With these equalities, it is possible to perform an integration of the dissipated power throughout the sphere

$$P_{\text{diss}} = \int_{-D/2}^{D/2} \int_{0}^{r_{\max}} \int_{0}^{2\pi} \frac{\sigma |E_\phi|^2}{2} r \, d\phi \, dr \, dx \qquad [10]$$

to find

$$P_{\text{diss}} = \frac{\pi (D/2)^5 \sigma \omega^2 B^2}{15} \qquad [11]$$

Incorporating all the above, P_{diss} in the sphere during application of a linear RF field B with a strength of 4μT is found to be 0.228 W. At this point, it is interesting to note that the energy required to tip the nuclei in the entire sphere by 90° at this field strength is only about 5.3 nJ, less than 1% of the energy dissipated when applying the 4μT linear field (2μT B_1^+, via Eq. 4) for 3 ms to produce a 90° pulse (11,12). Thus, of all the energy required to produce the field, less than 1% produces the desired nutation, with the vast majority producing nothing but an undesirable heating effect. Continuing, let us assume an experiment to image the entire sphere at an isometric resolution of 2 mm, or 0.008 cc voxel volume using a 128 × 128 in-plane matrix (resulting in an in-plane field of view of 256 mm in each direction) and 128 slices with interleaved acquisition. Also, assume a minimum of 10 ms time required per repetition per slice for pulses, encoding, and acquisition, a 50 kHz receiver bandwidth, very long repetition time (TR at least 1280 ms if all slices are interleaved) and short echo time (TE) so T_1 and T_2 effects are negligible, and a 90° pulse. With $\gamma = 42.58$ MHz and $B_1^+ = 2\mu T$, a pulse of approximately 3 ms will, therefore, induce a 90° pulse, giving our sequence a 30% duty cycle. Assuming M_0 of pure water (3.25×10^{-3} A/m times B_0) (4) and $B_1^- = 2\mu T$ (Eq. 4), we can calculate a signal strength of 2.78×10^{-8} V for a single voxel and an root mean square noise value of 1.36×10^{-8} V from the entire sphere. With 128 acquisitions on each plane, we gain a factor of $\sqrt{128}$, bringing the S/N to about 23.1. From the power absorbed during the pulse, the duty cycle for the interleaved sequence, and the density of the tissue (assume just 1000 kg/m^3 for this example), we can calculate the sphere-average SAR to be 0.0387 W/kg. Note that with Eqs. 4a and 4b, we find that if B_x is 4μT and B_y is 0, both B_1^+ and B_1^- will have magnitudes of 2μT, so the effects of using a linear or quadrature coil on SNR and SAR are considered implicitly in the equations given here as long as P_{diss} and B_1^- are calculated correctly.

From this simple example, it is possible to make some extrapolations within the regime where frequency is low enough that wavelength effects are not apparent and high enough that coil noise is negligible. In this regime, Eqs. 8 and 10 indicate that SAR and P_{diss} should be proportional to the square of the B_1 field frequency (or B_0 field strength) and with Eq. 3 and the proportionality between M_0 and B_0, SNR should be proportional to the B_1 field frequency (or B_0 field strength). Thus, at higher field strength, SNR would become more reasonable at this resolution. While the SAR, for this example, is very low compared to the existing head average limit of 3.2 W/kg (7), SAR for a fast spin echo sequence with shorter pulse durations at higher field strength could easily exceed this limit (13). In the event that a quadrature coil producing a perfectly homogeneous circularly polarized field was used in place of the linear with appropriate quadrature splitter/combiner for effective use in transmission and reception, an increase in SNR by a factor of $\sqrt{2}$ could be expected, and half the power would be required, also reducing SAR by a factor of 2 (14,1). In the case that a local surface coil was used for reception rather than a homogeneous volume coil, $B_1^-/\sqrt{\text{Pabs}}$ of the receive coil would be expected to be much higher in regions near the coil than in the homogeneous case, resulting in much higher SNR near the coil but lower SNR far from it, and in the case that multiple surface coils were used with separate receive chains, SNR would be a function of how the signal from these coils was combined (see references in the following section about parallel reception) but also generally higher near the coils and lower far from them. If an inhomogeneous transmit field were used, the signal intensity distribution would also vary accordingly across the sample. Changing nothing about our example but switching to a 3D acquisition and keeping all else the same would require much more time (due to holding TR constant at a very long value) but would also afford another factor of $\sqrt{128}$, bringing the S/N to about 262. In addition, acquiring multiple images and averaging them together would increase SNR by the square root of the number of averages.

Given the numerous tissue properties and imaging parameters that affect SNR (T_1, T_2, TE, TR, resolution, number of acquisitions and averages, method of reconstruction, etc.) for engineering purposes it is often desirable to define quantities that are dependent on the field distributions alone. This has led to the concept of "intrinsic SNR," which can be expressed in a number of ways depending on the purpose (15–17). It is also important to note that for receive coils the quantity $|B_1^-|/\sqrt{P_{\text{diss}}}$ is very relevant to performance, as is $|B_1^+|/\sqrt{P_{\text{diss}}}$ for a transmit coil.

Need for Advanced RF Field Calculations in MRI

The previous example served to illustrate in principle how field calculations can be used to predict and understand a wide range of factors important in conventional full *k*-space MRI. For realistically simulating actual coil geometries, anatomically accurate sample geometries, and the wide variety of image acquisition and reconstruction methods in application and in development today, numerical methods are often preferred. Here, we describe some of the departures from the simple illustration that require more complete consideration.

Although it may desirable in many cases to have perfectly homogeneous circularly polarized fields in transmission and in reception, in reality, this is difficult or impossible to achieve. One reason for this is that electrical currents induced in conductive tissue by the time-varying RF fields affect the field distribution. One result of tissue conductivity is decreased penetration (a "skin-depth" related effect), and another is spatial asymmetry

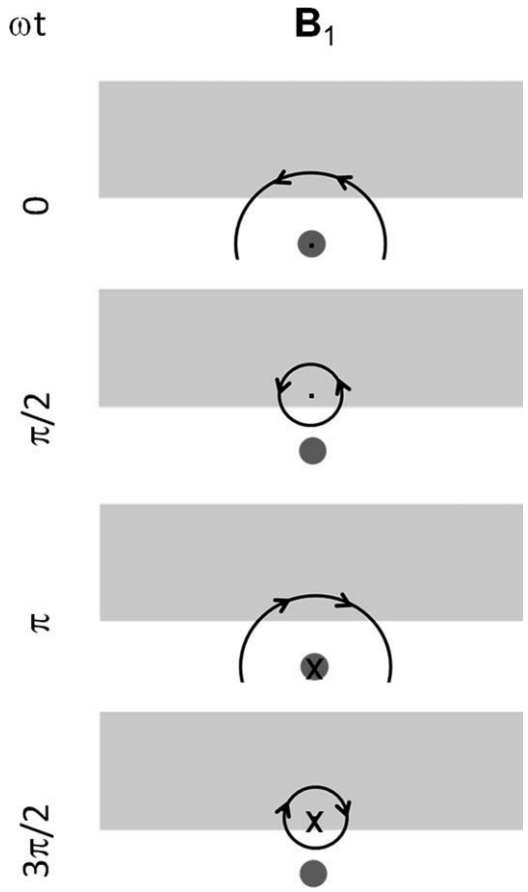

FIG. 5. Conceptual illustration of why B_1^+ and B_1^- can each be asymmetric and tend toward different sides of a coil even when the coil and sample are perfectly symmetric. Neglecting wavelength effects, currents induced in the conductive sample light gray by fields from the current element (dark gray) produce fields that both lag those from the coil and are oriented differently such that at the locations of the arrows, the field is seen to rotate primarily in the clockwise direction on the right side and in the counter-clockwise direction on the left.

in circularly polarized field components, even for perfectly symmetric samples and coils. The skin depth effect is well characterized elsewhere. The asymmetry effect can be understood by recognizing that (in the absence of wavelength effects) the magnetically induced "eddy" currents in the sample lag the currents in the coil by approximately 90° in phase (Eq. 8–Faraday's Law). Figure 5 shows conceptually what can happen in this situation, where the orientation of the fields due to the coil currents at some times and due to the eddy currents at others can result in a dominant direction of field rotation that is opposite on opposite sides of the coil.

Another reason that the creation of homogeneous fields is difficult or impossible is due to the dielectric currents in tissue giving rise to wavelength effects. Wavelength effects are more prominent at high frequencies. At 300 MHz, for example, the electromagnetic wavelength in brain tissue is approximately 13.4 cm. As such, fields propagating from multiple current elements in a single coil can interfere constructively in some places and destructively in others, producing spatially inhomogeneous excitation and reception distributions so that image intensity will be a function of the RF field pattern rather than only patient anatomy. In the case of array coils, interference from fields from different coils is a problem in transmission where coils are driven to produce fields simultaneously, but in reception, if the coils are adequately decoupled, there is effectively no interference from separate coils affecting the signal reception distributions.

Although analytical and semianalytical methods can be used to predict various global trends to some degree of accuracy, there are often significant departures from results acquired with these methods and those acquired with high-resolution anatomical models and fully numerical methods. One excellent example is with local SAR. Although it has been mentioned that the electrical field distribution calculated in a homogeneous phantom is not unlike that calculated for a high-resolution model of the human body (18), it is quite a different case for SAR (12). SAR is weighted heavily by tissue electrical conductivity, which varies by more than an order of magnitude between various tissues (19). Figure 6 shows an example of the SAR distribution on a transverse plane through the human head. Calculations of local SAR for a homogenous sphere and an anatomical model of the human head show the values to be up to three times higher in the model of the human head (13). This can be attributed to locally constrained current patterns due to inhomogeneous structures resulting in focal heating (20).

Finally, given a coil with specific geometry, circuitry, and drive location, perturbation of the field distribution will necessarily affect the impedance of the coil as a whole but also will affect the impedance of different portions in different ways and thus affect the very current and electrical distributions on the coil that create the fields to begin with. For this reason, when it is desired to model the behavior of a specific RF coil, it can be advisable to model the coil as accurately as possible in terms of geometry, circuitry, and drive location. Although in some cases the effects of adding such

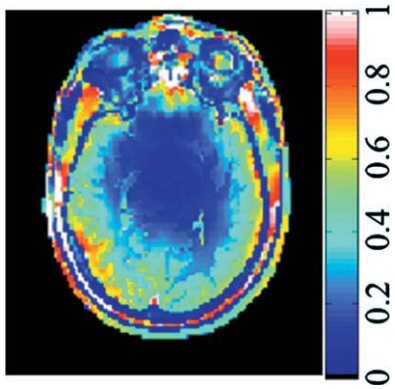

FIG. 6. SAR distribution on a transverse plane through the human head at 125 MHz. Dependence of SAR on tissue conductivity is clearly apparent, with low SAR in nonconductive tissues such as cortical bone and fat. Effects on SAR of even smaller differences, such as those between white and gray matter are also apparent.

considerations are not seen to be significant (21), in others they can be (22).

METHODS OF RF FIELD CALCULATION USED IN MRI WITH CONSIDERATION OF THE SAMPLE

Here, we will briefly review some of the wide variety of methods used to calculate RF electromagnetic fields in MRI with reference to examples in the literature. It is beyond the scope of this work to discuss implementation of these methods in detail.

Through the years, simple analytical calculations not unlike that shown previously in this work have yielded great insight into expected and observed trends in MRI signal, noise, and safety. Before beginning to discuss fully numerical approaches, it is important to note that computer-based implementation of analytically derived equations for electromagnetic fields in fairly simple shapes are often found very valuable to this day (17,23).

Compared to slabs, cylinders, infinitely long extrusions, spheres or spheroids of any number of layers, the human body is extremely complex, and coming up with representations of it in three-dimensional space is by itself a challenging task. Some early methods relied on infinitely long extrusions of fairly high-resolution cross-sectional images (24) or relatively simple low-resolution three-dimensional representations (25). More recently, a number of models have been produced based on image data and/or high-resolution photographic data of the interior of the human body from cadavers (21,26), followed by manually intensive segmentation of spatial information into a finite number of tissue types. While some models of portions living humans have been created through the years (27–30), including even a section of a mother and fetus (31), recently impressive efforts including high-resolution whole-body imaging of human subjects in vivo followed by labor-intensive manual segmentation have yielded an increasing number of high-resolution models of the entire human body (32,33). Because of the image-based nature of the data acquired and segmented to produce models of the human body, these models are most often represented as a distribution of a finite number of tissues at locations on a regular three-dimensional grid.

The human body has extremely complex geometry of weakly conductive material that today is most readily represented on a high-resolution regular three-dimensional grid. This makes the finite difference time domain method and related finite integration technique popular methods for performing RF EM calculations considering the human body. These methods can be arranged to step through space and time, solving single equations for single unknown values with reference only to neighboring locations in space and immediately previous points in time. As such they require relatively little memory for a given complex geometry and are excellent candidates for parallel computation. Although representation of good conductors (especially RF coils for MRI constructed of thin, smoothly varying shapes with faces in arbitrary orientation) on a Cartesian grid can lead to inaccurate results, a variety of advances in gridding and meshing are allowing for increasing accuracy in this area (34).

Other methods including the method of moments and the finite element method are very good for creating accurate representations of good conductors of arbitrary geometry but rely on methods such as matrix inversion, which work best for sparsely populated spaces. Finite element representations of the human body are used occasionally in MRI (35,36), but due to the computational requirements, the representations tend to have far more homogeneous representations of far fewer tissue types than finite difference time domain methods can accommodate on a given system. To represent both the RF coils and human body accurately in the same simulation, some groups have devised hybrid methods combining more than one method and sharing results between them (37).

APPLICATIONS FOR RF FIELD CALCULATIONS IN MRI

RF simulations are used for a wide variety of purposes in MRI today. Historically, they have been used to explain observed phenomena, predict and explore future trends, and ensure RF safety. Increasingly, they are used for design of RF coils, RF pulses, and image reconstruction methods.

Understanding and Explaining Observed Phenomena

Given the number of parameters that can affect MR images and the fairly complex relationship between the RF field distributions and the final images, use of simulations to explain observed phenomena and thus gain insight for how to improve results plays an important role. Some examples include demonstration of the need to consider the field component rotating opposite nuclear precession in signal reception (1–3), and assessing the importance of dielectric resonance and constructive/destructive interference in image intensity patterns seen in high field MRI (38–40).

Exploring Possibilities

A common theme in field calculations has been the prediction of future trends. Because SNR is expected to increase with B_0 field strength and B_1 field frequency, one seemingly constant trend is that toward higher field strengths. As mentioned in our simple illustration, for a range of frequencies where sample noise is dominant and the RF field pattern does not vary much with the B_1 frequency, SNR is expected to increase linear with B_0 while SAR will increase quadratically with B_0. In high-field MRI, however, the RF field pattern is very much a function of B_1 frequency and a number of departures from this excitation can be predicted depending on sample properties, sample geometries, region of interest, how excitations are defined, use of receive arrays, and a variety of other factors (12,16,17,41–43).

Effects of Parallel Reception

Simultaneous signal reception through multiple coils is the standard on most human MRI systems today. The signal from these receive coils can be combined in a very wide variety of ways (44–47), usually to maximize some

combination of SNR, resolution, and imaging speed. When a single RF coil is used in reception, noise is distributed evenly throughout the image, but when multiple coils are used, how the signal from multiple coils is acquired and combined has implications regarding the distributions of signal intensity (which can often be compensated for in postprocessing) and SNR (44,46,47). If a full *k*-space acquisition is made with multiple coils, it is possible to have evenly distributed noise in the final image by using a sum-of-magnitudes reconstruction (44). Often today, however, multiple coils are used to accelerate the imaging process by (in essence) skipping lines in *k*-space and (one way or another) using the different spatial distributions of the RF fields from the different coils to accomplish part of the spatial encoding—a process termed parallel imaging. Methods for using RF field calculations to predict SNR distributions have been developed for the Sensitivity Encoding (SENSE) method of parallel imaging using information about the magnetic fields and electric fields from each coil throughout the sample, as well as information about the encoding of spatial information through time (17,46,48), but this specific approach is not necessarily directly applicable to other parallel imaging methods in general. Currently, experimental methods are more often used to assess SNR of different parallel imaging methods (49), but increasingly sophisticated MRI simulation tools that consider accurate RF electromagnetic field distributions in both simulation of signal and noise (50,51) may be found useful for designing and evaluating competing methods in the future. One important concept in all methods of parallel imaging is that of correlated noise. Random motion of ions and dipoles in the sample will induce currents in all of the receive coils simultaneously, with magnitude and phase dependent on the electric field distribution associated with each coil (46,48). For an array of N coils, an N by N noise resistance matrix having values $R_{l,m}$ (l and m each equal 1 to N) representing correlated noise between each coil pair can be calculated with the electric field distributions of all coils and the conductivity distribution of the sample (44,46).

$$R_{l,m} = \int \sigma \mathbf{E}_l \cdot \mathbf{E}_m dV \qquad [12]$$

Again, how exactly these values affect SNR in parallel imaging depends on the specific method of acquisition and reconstruction.

Transmit Arrays

Single coils used to excite entire volumes typically have equal and opposite currents on opposite sides of the sample at any given time. In many samples (including the human head), this leads to a situation where magnetic fields interfere constructively near the center of the object and destructively roughly a quarter-wavelength away (39,40). Use of multiple coils in transmission allows for variation of the magnitude and phase of the RF field through space and time on a patient-specific basis. Though it is at present largely experimental technology on a growing number of research systems, this technology has been used effectively to improve homogeneity of transmit field distributions (29,42,52), reduce SAR (53), and shorten the duration of RF-tailored pulses (54). Numerical field calculations have been used extensively in the exploration of possibilities for this technology (18,23,29,55–70). The simplest approach for using transmit arrays is to vary the magnitude and phase in various elements to achieve a homogeneous distribution of the B_1^+ field magnitude, and then use this more homogeneous distribution in standard pulses throughout the sequence. This approach has come to be known as "RF shimming" or "B_1 shimming." Approaches using different waveforms in the separate channels to achieve a variety of aims including acceleration of spatially selective tailored RF pulses have become known as "parallel transmission." These methods will be discussed briefly in the "pulse design" section below. Figure 7 shows simulated images in the head at 7T to demonstrate how the progression from a single volume coil in transmission and reception to use of a volume coil in transmission and array in reception to, finally, use of a transmit/receive array with RF shimming can markedly improve image homogeneity.

Safety Assurance

To ensure safety, limits are placed on the amount of heating and/or temperature achieved in the entire body, the portion of the body within the effective volume of the coil, the patient head, and in any 10 g local region of the body (7). Although it is reasonable to limit the amount of RF energy absorbed in any local region, it is difficult or impossible to measure this quantity throughout the body and thus numerical calculations are used increasingly to determine the limits for safe usage of specific MRI coils. Because whole-body, head, and partial body average SAR values can be estimated with conventional means (e.g., real-time hardware-based estimates of RF power dissipated in the subject divided by the mass of the subject), a valuable quantity from calculations is the ratio of maximum local SAR to whole-body average SAR. Several authors have published calculations of SAR designed to compare directly to the established limits (12,13,21,27,43,66,71–78). In a few cases, calculations of the SAR distributions have been used in calculation of temperature increase, which is more directly related to the risks of RF energy deposition (27,31,33,72,75–80).

Numerical calculations of local SAR levels are now performed routinely in industry, and their results guide the operation of modern MRI systems in practice. In one implementation, a large array of calculations is performed for a wide variety of body models in a complete range of possible locations within each available transmit coil for a given system, and results are calibrated to real time data on time-average power and/or RF magnetic field applied and subject mass. Indeed, it has been shown that SAR levels and distributions are very dependent on patient location in the magnet and subject body morphology (21,78). Additional variables that are not as readily adjusted include posture of the body (79) (Fig. 8), and model resolution (71,80). Although an early study indicated relatively little dependence of local SAR

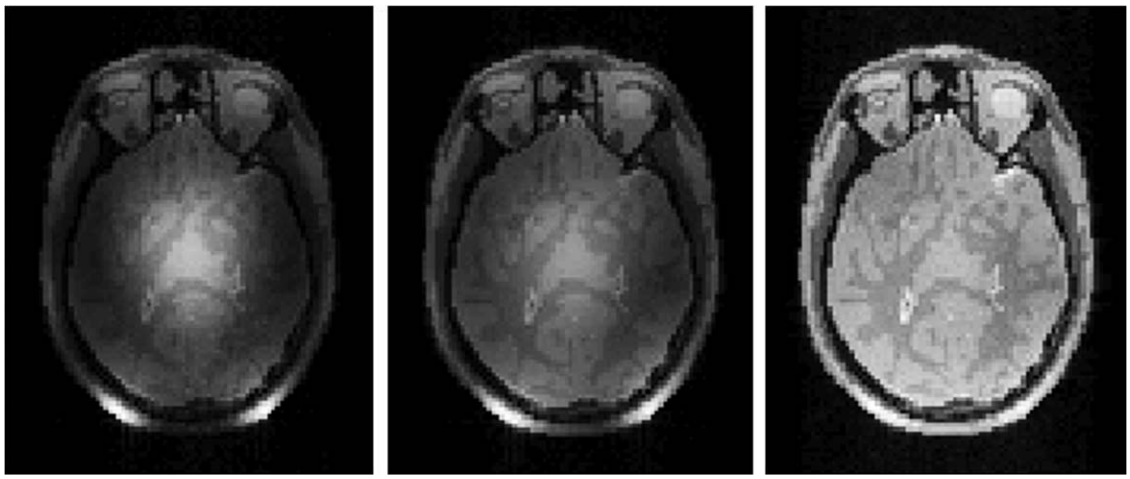

FIG. 7. Simulated MR images showing the results of different coil configurations at 300 MHz (7T). Use of a single volume coil in both transmission and reception (left) results in relatively strong B_1^+ and B_1^- fields near the center (due to constructive interference) surrounded by weaker fields (due do destructive interference) resulting in a center-bright appearance of the signal intensity distribution. Use of a single volume coil in transmission but an array of decoupled coils in reception with sum-of-magnitude reconstruction (center) results in relatively strong B_1^+ near the center but relatively strong B_1^- near the periphery resulting in a more homogeneous signal intensity distribution. Use of a transmit array with RF shimming to lessen the pattern of constructive and destructive interference in transmission and a receive array with sum-of-magnitude reconstruction (right) produces a very homogeneous image, even at this high frequency with only eight elements in transmission and reception. Figure was created with a freely available MR system simulator (51).

levels on model resolution (71), more recently at least one study indicated that up to $(2\ \text{mm})^3$, a higher model resolution would produce a higher local (10 g) SAR level for a given RF magnetic field strength, and also a higher ratio of local-to-global SAR (80). A possible explanation is seen in the ability to better resolve high SAR levels near boundaries of dissimilar tissues with a higher resolution model, in which case it is possible that the earlier study mentioned showed little relation between local SAR and model resolution because the maximum local (1 g) SAR in that case occurred in the vitreous humor of the eye, where anatomy is relatively featureless. Although it requires further study, a work examining the effect of model resolution on calculated temperature increase for a given RF magnetic field strength showed a lower dependence than that seen for local SAR but also a decreasing maximum local temperature change with increasing model resolution despite the increase in local SAR (80). If future studies agree with this finding, a possible explanation may be in a better representation of the moderating effect of thermal conduction at the higher resolution.

While MRI is now a standard tool in medicine, a portion of the patient population having some types of implanted passive and active devices is excluded from receiving what would be standard-of-care for other patients due to safety concerns. The static, switched, and RF fields in MRI can all interact with implanted devices resulting in adverse effects. The use of numerical calculation methods to examine interactions of RF fields with implanted devices is increasing in recent years (30,81,82). Of particular interest is the high local heating expected at the tip of a wire in contact with or implanted into tissue (as for a pacemaker or deep brain stimulator) or conductive catheter (81,82). Efforts to

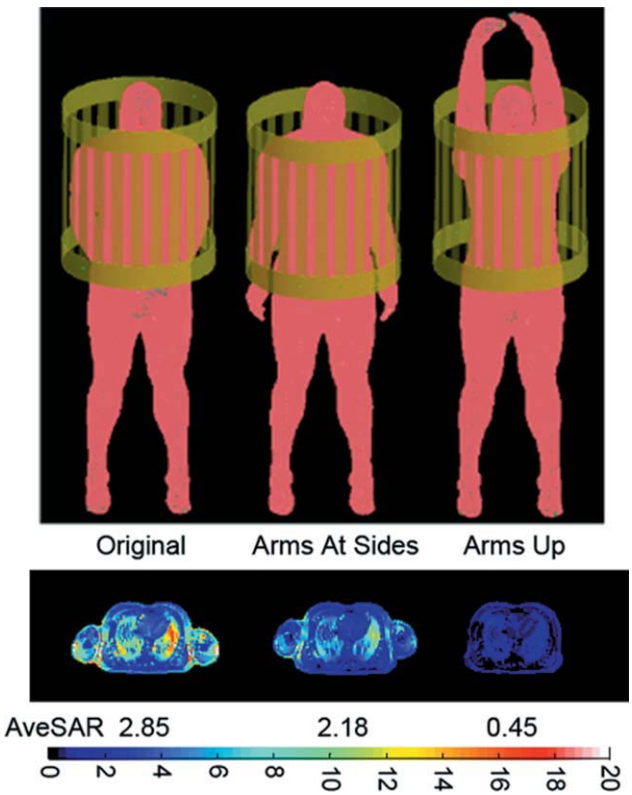

FIG. 8. Geometry of a human body model in various postures (top) and corresponding SAR distribution (bottom). Color scale is for single-cell $(5\ \text{mm})^3$ SAR. Whole-body average SAR is also given below the SAR plot for each case. In all cases, the fields are driven to produce a $2\mu\text{T}$ B_1^+ at the center of the heart and a large, cylindrical RF shield was included in simulation (79). All values are in W/kg.

produce MRI-compatible devices have led to increasingly sophisticated designs in these wires resulting in relatively complex geometries (83). Although modeling such complex geometries presents definite challenges, numerical modeling methods are sure to have a place in the continued design of devices.

RF Coil Design

RF field calculations have been used for decades in the design and evaluation of different general RF coil geometries without consideration of the human body. More recently, interaction of the fields with the body has become a major factor—especially in high field MRI. Some current popular examples include transmit arrays (discussed previously) and "traveling wave MRI" (10,84–88). Besides consideration of general coil geometry, field calculations are used increasingly in making subtle changes in geometry and even optimize effects of circuitry on the field distributions in the presence of a load (89).

Advanced Pulse Design

Brief discussion of the use of multiple transmit coils for RF shimming was given previously. With any number of RF coils, it is increasingly difficult to achieve homogeneous RF magnetic field distributions in the human body at increasing B_1 frequency due to limitations of what can be imposed within the limits of the Maxwell equations (90). Nonetheless, through the past decades researchers have developed a variety of methods to achieve excitations in space that are distributed quite differently than the RF fields alone. With careful control of the RF and gradient waveforms through time, it is possible to achieve excitations that are either more homogeneous than the applied RF fields, or contain much higher spatial selectivity than could be achieved using only RF fields with wavelengths on the order of several centimeters. These pulses often require longer durations and higher SAR than more conventional pulses, but the flexibility afforded with transmit arrays can be used to improve either of these limitations (60–62,69,70). As seen in Eq. 2, it is clear that not only the time courses and spatial distribution of the applied (RF and gradient) fields but also inhomogeneity in the static magnetic field and chemical shift of different nuclei in the tissue affect nuclear excitation. With strategic pulse design, it is also, thus, possible to compensate for B_0 inhomogeneity (91).

Other Applications

The above attempt to categorize applications of RF field calculations considering the human body for MRI does not allow for inclusion of all ongoing work. For example, although it is not a safety issue in MRI, a recently published article presented a model of the mechanism for the known biological effect of RF hearing in MRI (92). In addition, a number of recent works have explored the ability to tailor the RF fields in MRI by strategic positioning of dielectric materials rather than use of specialized coils (93,94).

MRI-BASED MEASUREMENT OF ELECTROMAGNETIC FIELDS

For anyone concerned with electromagnetic field distributions in matter, it is important to note that MRI can be used as a field measurement tool. Because the MRI signal is sensitive to the fields throughout the sample or subject, studies can be designed to isolate the effects of any of these. Thus, MRI is a potential tool for validating field simulations or even measuring fields and their effects directly. Important examples are seen in MRI-based measurement of the distribution of static magnetic fields (95) and the pertinent circularly polarized components of RF magnetic fields (40). MRI-based methods for measuring the RF magnetic fields have received much attention and advancement in recent years due to the increasing utility and prevalence of, first, receive arrays and, more recently, transmit arrays in MRI. Because changes in temperature and even absolute temperature can be measured with MR-based techniques, in some cases, this can be used to evaluate the SAR distribution (96–98). With some careful study design, acquisition, and analysis, static or RF current densities (99,100) and even RF electrical (101) and magnetic (102) properties of the sample can be measured in some circumstances.

SUMMARY

Because of the complex interactions between RF fields and the human body in MRI, field calculations are increasingly important in design of techniques and technology for the future, as well as in safety assurance of current methods in MRI. In this work, the basic concepts and necessities for performing RF field calculations for MRI were explained before review of current applications in the hope that a reader not having expertise in both might gain confidence toward contributing to this area of study. Other recent review articles that may be of interest include a comprehensive review of field calculations in the human body for a wide variety of purposes including MRI (103) and a more comprehensive catalog of recent publications presenting field calculations in MRI (104).

REFERENCES

1. Hoult DI. The principle of reciprocity in signal strength calculations—a mathematical guide. Concepts in Magnetic Resonance 2000;12:173–187.
2. Glover GH, Hayes CE, Pelc NJ, Edelstein WA, Mueller OM, Hart HR, Hardy CJ, O'Donnell M, Barber WD. Comparison of linear and circular polarization for magnetic resonance imaging. J Magn Reson 1985;64:255–270.
3. Collins CM, Yang QX, Wang JH, Zhu X-H, Adriany G, Michaeli S, Vaughan JT, Zhang X, Liu H, Anderson P, Ugurbil K, Smith MB, Chen W. Different excitation and reception distributions with a single-loop transmit-receive surface coil near a head-sized spherical phantom at 300 MHz. Magn Reson Med, 2003;47:1026–1028.
4. Hoult DI, Lauterbur PC. The sensitivity of the zeugmatographic experiment involving human samples. J Magn Reson 1979;34: 425–433.
5. Haacke EM, Brown RW, Thompson MR, Venkatesan R (1999). Magnetic resonance imaging: physical principles and sequence design. New York: Wiley; p 47.
6. Park BS, Neuberger T, Webb AG, Bigler DC, Collins CM. Faraday shields within a solenoidal coil to reduce sample heating: numerical comparison of designs and experimental verification. J Magn Reson 2010;202:72–77.

7. IEC (2010). International standard, medical equipment—part 2: particular requirements for the safety of magnetic resonance equipment for medical diagnosis, 3rd ed. International Electrotechnical Commission: Geneva; 2010. 601–2-33.
8. Foster KP, Schwan HP. Dielectric properties of tissues and biological materials: a critical review. Crit Rev Biomed Eng 1989;17: 25–104.
9. Keltner JR, Carlson JW, Roos MS, Wong TS, Wong TL, Budinger TF. Electromagnetic fields of surface coil in vivo NMR at high frequencies. Magn Reson Med 1991;22:467–480.
10. Brunner DO, De Zanche N, Fröhlich J, Paska J, Pruessmann KP. Travelling-wave nuclear magnetic resonance. Nature 2009;457: 994–999.
11. Abragam A. Principles of nuclear magnetism. Oxford: Oxford University Press; 1961. pp 71–72.
12. Collins CM, Smith MB. Signal-to-noise ratio and absorbed power as functions of main magnetic field strength and definition of "90°" RF pulse for the head in the birdcage coil. Magn Reson Med 2001; 45:684–691.
13. Collins CM, Li S, Smith MB SAR and B1 field distributions in a heterogeneous human head model within a birdcage coil. Magn Reson Med 1998;40:847–856.
14. Hoult DI, Chen C-N, Sank VJ. Quadrature detection in the laboratory frame. Magn Reson Med 1983;1:339–353.
15. Edelstein WA, Glover GH, Hardy CJ, Redington RW. The intrinsic signal-to-noise ratio in NMR imaging. Magn Reson Med 1986;3: 604–618.
16. Ocali O, Atalar E. Ultimate intrinsic signal-to-noise ratio in MRI. Magn Reson Imaging 1998;39:462–473.
17. Wiesinger F, Boesiger P, Pruessmann KP. Electrodynamics and ultimate SNR in parallel MR Imaging. Magn Reson Med 2004;52: 376–390.
18. van den Berg CAT, van den Bergen B, van de Kamer JB, Raaymakers BW, Kroeze H, Bartels LW, Lagendijk JJW. Simultaneous B_1^+ homogenization and specific absorption rate hotspot suppression using a magnetic resonance phased array transmit coil. Magn Reson Med 2007;57:577–586.
19. Gabriel, C. Compilation of the dielectric properties of body tissues at RF and microwave frequencies. Air Force materiel command, Brooks Air Force Base, Texas: AL/OE-TR-1996–0037.
20. Davis PL, Shang C, Talagala L, Pasculle AW. Magnetic resonance imaging can cause focal heating in a nonuniform phantom. IEEE Trans Biomed Eng 1993;40:1324–1327.
21. Liu W, Collins CM, Smith MB. Calculations of B1 distribution, specific energy absorption rate, and intrinsic signal-to-noise ratio for a body-size birdcage coil loaded with different human subjects at 64 and 128 MHz. Appl Magn Reson 2005;29:5–18.
22. Ibrahim T, Lee R, Baertlein BA, Yu Y, Robitaille PML. Computational analysis of the high pass birdcage resonator: finite difference time domain simulations for high-field MRI. Magn Reson Imaging 2000;18:835–843.
23. Lattanzi R, Grant AK, Sodickson DK, Zhu Y. Electrodynamic constraints on minimum SAR in parallel excitation. In Joint Annual Meeting ISMRM-ESMRMB, May 19–25, Berlin, 2007; p 675.
24. Smith MB, Ashtiani CN, Cendes ZJ, Williams GD, Martin JT. Finite element calculation of radiofrequency magnetic fields in simulated human organs. In Book of abstracts, SMRM 8th Annual Meeting and Exhibition; Amsterdam, (The Netherlands); 1989. p 995.
25. Chatterjee I, Hagmann MJ, Gandhi OP. Electromagnetic-energy deposition in an inhomogeneous block model of man for near-field irradiation conditions. IEEE Trans Microwave Theory Tech 1980;28: 1452–1459.
26. Dimbylow PJ. FDTD calculations of the whole-body averaged SAR in an anatomically realistic voxel model of the human body from 1 MHz to 1 GHz. Phys Med Biol 1997;42:479–490.
27. Hand JW, Lau RW, Lagendijk JJW, Ling J, Burl M, Young IR. Electromagnetic and thermal modeling of SAR and temperature fields in tissue due to an RF decoupling coil. Magn Reson Med 1999;42:183–192.
28. Collins CM, Yang B, Yang QX, Smith MB. Numerical calculations of the static magnetic field in three-dimensional multi-tissue models of the human head. Magn Reson Imaging 2002;20:413–424.
29. Ibrahim TS, Lee R, Baertlein BA, Abduljalil AM, Zhu H, Robitaille PL. Effect of RF coil excitation on field inhomogeneity at ultra high fields: a field optimized TEM resonator. Magn Reson Imaging 2001; 19:1339–1347.
30. Angelone LM, Potthast A, Segonne F, Iwaki S, Belliveau JW, Bonmassar G. Metallic electrodes and leads in simultaneous EEG-MRI: specific absorption rate (SAR) simulation studies. Bioelectromagnetics 2004;25:285–295.
31. Hand JW, Li Y, Thomas EL, Rutherford MA, Hajnal JV. Prediction of specific absorption rate in mother and fetus associated with MRI examinations during pregnancy. Magn Reson Med 2006;55:883–893.
32. Christ A, Kainz W, Hahn EG, Honegger K, Zefferer M, Neufeld E, Rascher W, Janka R, Bautz W, Chen J, Kiefer B, Schmitt P, Hollenbach H-P, Shen J, Oberle M, Szczerba D, Kam A, Guag JW, Kuster N. The virtual family—development of surface-based anatomical models of two adults and two children for dosimetric simulations. Phys Med Biol 2010;55:23–38.
33. Wu D, Shamsi S, Chen J, Kainz W. Evaluations of specific absorption rate and temperature increase within pregnant female models in magnetic resonance imaging birdcage coils. IEEE Trans Microw Theory Tech 2006;54:4472–4478.
34. Zagorodnovny IR, Schuhmann R, Weiland T. A uniformly stable conformal FDTD-method in Cartesian grids. Int J Numer Model 2003;16:127–141.
35. Vogel MH, Kleihorst RP. Large-scale simulations including a human model for MRI. In IEEE MTT-S 2007 International Microwave Symposium Technical Program, Honolulu, June 3–8, 2007; pp 1010.
36. Cloos MA, Luong M, Ferrand G, Amadon A, LeBihan D, Boulant N. Local SAR reduction in parallel excitation based on channel-dependent tikhonov parameters. J Magn Reson Imaging 2010;32: 1209–1216.
37. Li BK, Liu F, Crozier S. Focused, eight-element transceive phased array coil for parallel magnetic resonance imaging of the chest — theoretical considerations. Magn Reson Med 2005;53:1251–1257.
38. Tropp J Image brightening in samples of high dielectric constant. J Magn Reson 2004;167:12–24.
39. Collins CM, Liu W, Schreiber W, Yang QX, Smith MB. Central brightening due to constructive interference with, without, and despite dielectric resonance. J Magn Reson Imaging 2005;21:192–196.
40. Van de Moortele P-F, Akgun C, Adriany G, Moeller S, Ritter J, Collins CM, Smith MB, Vaughan JT, Ugurbil K. B1 interferences and spatial phase patterns at 7 tesla with a head transceiver array coil. Magn Reson Med 2005;54:1503–1518.
41. Singerman RW, Denison TJ, Wen H, Balaban RS. Simulation of B_1 field distribution and intrinsic signal-to-noise in cardiac MRI as a function of static magnetic field. J Magn Reson 1997;125:72–83.
42. Hoult DI. The sensitivity and power deposition of the high field imaging experiment. J Magn Reson Imaging 2000;12:46–67.
43. Collins CM, Smith MB. Calculations of B_1 distribution, SNR, and SAR for a surface coil against an anatomically-accurate human body model. Magn Reson Med, 2001;45:692–699.
44. Roemer PB, Edelstein WA, Hayes CE, Souza SP, Mueller OM. The NMR phased array. Magn Reson Med 1990;16:192–225.
45. Sodickson DK, Manning WJ. Simultaneous acquisition of spatial harmonics (SMASH): ultra-fast imaging with radiofrequency coil arrays. Magn Reson Med 1997;38:591–603.
46. Pruessmann KP, Weiger M, Scheidegger MB, Boesiger P. SENSE: sensitivity encoding for fast MRI. Magn Reson Med 1999;42: 952–962.
47. Griswold MA, Jakob PM, Heidemann RM, Nittka M, Jellus V, Wang J, Kiefer B, Haase A. Generalized autocalibrating partially parallel acquisitions (GRAPPA). Magn Reson Med 2002;47:1202–1210.
48. Wiesinger F, van de Moortele P-F, Adriany G, De Zanche N, Ugurbil K, Pruessmann KP. Parallel imaging performance as a function of field strength—an experimental investigation using electrodynamic scaling. Magn Reson Med 2004;52:953–964.
49. Robson PM, Grant AK, Madhuranthakam AJ, Lattanzi R, Sodickson DK, McKenzie CA. Quantification of SNR and g-factor for parallel MRI: universal application to image-based and k-space-based image recnstructions. Proc Int Soc Magn Reson Med 2008;16:p1295.
50. Bankson JA, Wright SM. Simulation-based investigation of partially parallel imaging with a linear array at high accelerations. Magn Reson Med 2002;47:777–786.
51. Cao Z; Sica CT, Oh S, McGarrity J, Horan T, Park B, Collins CM. An MRI simulator for effects of realistic field distributions and pulse sequences, including SAR and noise correlation for array coils. Proc: Stockholm, Sweden; 2010 ISMRM, p 1456.
52. Vaughan JT, DelaBarre L, Snyder C, Tian J, Akgun C, Shrivastava D, Liu W, Olson C, Adriany G, Strupp J, Andersen P, Gopinath A, van

de Moortele P-F, Garwood M, Ugurbil K. 9.4T Human MRI: preliminary results. Magn Reson Med 2006;56:1274–1282.
53. Metzger GJ, Snyder C, Akgun C, Vaughan JT, Ugurbil K, Van de Moortele P-F. Local B_1^+ shimming for prostate imaging with transceiver arrays at7T based on subject-dependent transmit phase measurements. Magn Reson Med 2008;59:396–409.
54. Katscher U, Börnert P, Leussler C, van den Brink JS. Transmit SENSE. Magn Reson Med 2003;49:144–150.
55. Li BK, Liu F, Crozier S. Focused, eight-element transceive phased array coil for parallel magnetic resonance imaging of the chest — theoretical considerations. Magn Reson Med 2005;53:1251–1257.
56. Collins CM, Liu W, Swift BJ, Smith MB. Combination of optimized transmit arrays and some parallel imaging reconstruction methods can yield homogeneous images at very high frequencies. Magn Reson Med 2005;54:1327–1332.
57. Li BK, Xu B, Liu F, Crozier S. Multiple-acquisition parallel imaging combined with a transceive array for the amelioration of high-field RF distortion: a modeling study. Concepts Magn Reson Part B—Magn Resone Eng 2006;29B:95–105.
58. Abraham R, Ibrahim TS. Proposed radiofrequency phased-array excitation scheme for homogenous and localized 7-Tesla whole- body imaging based on full-wave numerical simulations. Magn Reson Med 2007;57:235–242.
59. Collins CM, Wang Z, Mao W, Fang J, Liu W, Smith MB. Array-optimized composite pulses for excellent whole-brain homogeneity in high field MRI. Magn Reson Med 2007;57:470–474.
60. Xu D, King KF, Zhu Y, McKinnon GC, Liang Z-P. A noniterative method to design large-tip-angle multidimensional spatially-selective radio frequency pulses for parallel transmission. Magn Reson Med 2007;58:326–334.
61. Wu X, Akgun C, Vaughan JT, Ugurbil K, Van de Moortele P-F. SAR reduction in transmit SENSE using adapted excitation k-space trajectories. In Proceedings of the Joint Annual Meeting ISMRM-ESMRMB, Berlin, May 19–25; 2007. p 673.
62. Graesslin I, Biederer S, Schweser F, Zimmermann K-H, Katscher U, Börnert P. SAR reduction for parallel transmission using VERSE and K-space filtering. In Proceedings of the Joint Annual Meeting ISMRM-ESMRMB, Berlin, May 19–25; 2007. p 674.
63. Ibrahim TS, Tang L. A whole-body 7 Tesla RF excitation scheme with much improved B_1^+ field homogeneity and local/global SARs over quadrature excitation. In Proceedings of the Joint Annual Meeting ISMRM-ESMRMB, Berlin, May 19–25; 2007. p 1013.
64. Wang Z, Oh S-H, Smith MB, Collins CM. RF shimming considering both excitation homogeneity and SAR. In Proceedings of the Joint Annual Meeting ISMRM-ESMRMB, Berlin, May 19–25; 2007. p 1022.
65. Akgun CE, Snyder CJ, DelaBarre L, Tian J, van de Moortele P-F, Moeller S, Ugurbil K, Vaughan JT. A novel RF head coil for 7T homogeneity and parallel imaging applications. In Proceedings of the Joint Annual Meeting ISMRM-ESMRMB, Berlin, May 19–25; 2007. p 1031.
66. McKinnon G. RF shimming and SAR considerations with an eight-element 3T body coil. In Proceedings of the Joint Annual Meeting ISMRM-ESMRMB, Berlin, May 19–25; 2007. p 1085.
67. Graesslin I, Biederer S, Falaggis K, Vernickel P, Dingemans H, Mens G, Roeschmann P, Leussler C, Zhai Z, Morich M, Katscher U. Real-time SAR monitoring to ensure patient safety for parallel transmission systems. In Proceedings of the Joint Annual Meeting ISMRM-ESMRMB, Berlin, May 19–25; 2007. p 1086.
68. Collins CM, Wang Z, Smith MB. A conservative method for ensuring safety within transmit arrays. In Proceedings of the Joint Annual Meeting ISMRM-ESMRMB, Berlin, May 19–25; 2007. p 1092.
69. Zelinski AC, Setsompop K, Alagappan V, Gagoski BA, Angelone LM, Bonmassar G, Fontius U, Schmitt F, Adalsteinsson E, Wald LL. Pulse design methods for reduction of specific absorption rate in parallel RF excitation. In Proceedings of the Joint Annual Meeting ISMRM-ESMRMB, Berlin, May 19–25; 2007. p 1698.
70. Zelinski AC, Goyal VK, Angelone L, Bonmassar B, Wald LL, Adalsteinsson E. Designing RF pulses with optimal specific absorption rate (SAR) characteristics and exploring excitation fidelity, SAR and pulse duration tradeoffs. In Proceedings of the Joint Annual Meeting ISMRM-ESMRMB, Berlin, May 19–25; 2007. p 1699.
71. Collins CM, Smith MB. Spatial resolution of numerical models of man and calculated specific absorption rate using the FDTD method: a study at 64 MHz in a magnetic resonance imaging coil. J Magn Reson Imaging 2003;18:383–388.
72. Collins CM, Liu W, Wang JH, Gruetter R, Vaughan JT, Ugurbil K, Smith MB. Temperature and SAR calculations for a human head within volume and surface coils at 64 and 300 MHz. J Magn Reson Imaging 2004;19:650–656.
73. Hand JW, Li Y, Thomas EL, Rutherford MA, Hajnal JV. Prediction of specific absorption rate in mother and fetus associated with MRI examinations during pregnancy. Magn Reson Med 2006;55:883–893.
74. Zhai Z, DeMeester GD, Morich MA, Shvartsman SM, Kleihorst RP. Numerical evaluation of B_1^- field and SAR for heterogeneous and homogeneous body model. In Proceedings of the 12th Scientific meeting of the International Society for Magnetic Resonance in Medicine, Kyoto; 2004. p 666.
75. Nguyen UD, Brown JS, Chang IA, Krycia J, Mirotznik MS. Numerical evaluation of heating of human head due to magnetic resonance image. IEEE Trans Biomed Eng 2004;51:1301–1309.
76. Hand JW, Lagendijk JJW, Hajnal JV, Lau RW. Young IR. SAR and temperature changes in the leg due to an RF decoupling coil at frequencies between 64 and 213 MHz. J Magn Reson Imag 2000;12: 68–74.
77. Nadobny J, Szimtenings M, Diehl D, Stetter E, Brinker G, Wust P. Evaluation of MR-induced hot spots for different temporal SAR modes using a time-dependant finite-difference method with explicit temperature gradient treatment. IEEE Trans Biomed Eng 2007;54:1837–1850.
78. Renz W. MR systems safety strategies—RF heating hazards. In ISMRM Workshop Series 2010; MR Safety: RF Heating of the human in MRI. Stillwater, MN, October 15–17; 2010.
79. Wang Z, Penney CW, Luebbers RJ, Collins CM. Poseable male and female numerical body models for field calculations in MRI. In Proceedings of the 16th Scientific Meeting and Exhibition of the International Society for Magnetic Resonance in Medicine, Toronto, May 3–9; 2008. p 75.
80. Wang Z, Robb F, Collins C. The effect of human model resolution on numerical calculation of SAR and temperature in MRI. In Proceedings of the 17th Scientific Meeting and Exhibition of the International Society for Magnetic Resonance in Medicine, Honolulu, April 18–24; 2009. p 4797.
81. Yeung CJ, Susil RC, Atalar E. RF heating due to conductive wires during MRI depends on the phase distribution of the transmit field. Magn Reson Med 2002;48:1096–1098.
82. Bassen H, Kainz W, Mendoza G, Kellom T. MRI-induced heating of thin wire metallic implants—laboratory and computational studies—findings and new questions raised. Minim Invasive Ther Allied Technol 2006;15:76–84.
83. Bottomley PA, Edelstein WA, Kumar A, Allen JM, Karmarkar P. Towards MRI-safe implanted leads: a comparative evaluation of four designs. Proc Int Soc Mag Reson Med 2010;18:776.
84. Webb AG, Collins CM, Versluis MJ, Kan HE, Smith MB. MRI and localized proton spectroscopy in human leg muscle at 7 tesla using longitudinal traveling waves. Magn Reson Med 2010;63:297–302.
85. Lee DJ, Glover PM. A comparison of a patch antenna to an end-fire helix antenna for use in travelling wave MRI. Proc Int Soc Magn Reson Med 2010;18:431.
86. Andreychenko A, Voogt I, Kroeze H, Klomp DW, Lagendijk JJ, Luijten P, van den Berg CA. An advantageous combination of travelling wave and local receive for spine MR imaging at 7T: local SAR reduction and SENSE reconstruction. Proc Int Soc Mag Reson Med 2010;18:430.
87. B. Hu1, S. Farhat1, P. Glover. A horn antenna improves the transmit field homogeneity in the human brain using the travelling wave technique. Proc Int Soc Mag Reson Med. 2010;18:1481.
88. Zhang B, Sodickson DK, Duan Q, Wiggins G. Contribution of the inherent traveling wave in 7T to large FOV imaging. Proc Int Soc Magn Reson Med 2010;18:1480.
89. Kozlov M, Turner R. Fast MRI coil analysis based on 3-D electromagnetic and RF circuit co-simulation. J Magn Reson 2009;200: 147–152.
90. Mao W, Smith MB, and Collins CM. Exploring the Limits of RF Shimming for High-Field MRI of the Human Head. Magn Reson Med 2006;56:918–922.
91. Heilman JA, Derakhshan JJ, Riffe MJ, Gudino N, Tkach J, Flask CA, Duerk JL, Griswold MA. B0 and B1 correction using the inherent degrees of freedom of a multi-channel transmit array. In Proceedings of the 17th Scientific meeting of the International Society for Magnetic Resonance in Medicine: Honolulu, HI; 2009. p 251.

92. Lin JC, Wang Z. Acoustic pressure waves induced in human heads by RF pulses from high-field MRI scanners. Health Phys 2010;98: 603–613.
93. Yang QX, Mao W, Wang J, Smith MB, Lei H, Zhang X, Ugurbil K, Chen W. Manipulation of image intensity distribution at 7.0 T: passive RF shimming and focusing with dielectric materials. J Magn Reson Imaging 2006;24:197–202.
94. Teeuwisse WM, Collins CM, Wang C, Yang QX, Ma W, Smith NB, van Osch MJP, Webb AG. Improvement in high field pulsed arterial spin labelling using dielectric pads: a simulation and experimental study. In Proceedings of the 18th Scientific meeting of the International Society for Magnetic Resonance in Medicine: Stockholm; 2010, p. 3863.
95. Li S, Dardzinski BJ, Collins CM, Yang QX, Smith MB. Three-dimensional mapping of the static magnetic field inside the human head. Magn Reson Med 1996;36:705–714.
96. Shapiro EM, Borthakur A, Shapiro MJ, Reddy R, Leigh JS. Fast MRI of RF heating via phase difference mapping. Magn Reson Med 2002;47:492–498.
97. Cline H, Mallozzi R, Li Z, McKinnon G, Barber W. Radiofrequency power deposition utilizing thermal imaging. Magn Reson Med 2004; 51:1129–1137.
98. Oh S, Webb AG, Neuberger T, Park BS, Collins CM. Experimental and numerical assessment of MRI-induced temperature change and SAR distributions in phantoms and in vivo. Magn Reson Med 2010; 63:218–223.
99. Scott GC, Joy MLG, Armstrong RL, Henkelman RM. Sensitivity of magnetic-resonance current-density imaging. J Magn Reson Imaging 1992;97:235–254.
100. Scott GC, Joy MLG, Armstrong RL, Henkelman RM. RF current density imaging in homogeneous media. Magn Reson Med 28 186–201.
101. Katscher U, Hanft M, Vernickel P, Findeklee C. Experimental verification of electric properties tomography (EPT). Proc Int Soc Mag Reson Med 2006;14:3035.
102. de Rochefort L, Brown R, Prince MR, Wang Y. Quantitative MR susceptibility mapping using piece-wise constant regularized inversion of the magnetic field. Magn Reson Med 2008;60:1003–1009.
103. Hand JW. Modelling the interaction of electromagnetic fields (10 MHz–10 GHz) with the human body: methods and applications. Phys Med Biol 2008;53:R243–R286.
104. Collins CM. Numerical field calculations considering the human subject for engineering and safety assurance in MRI. NMR Biomed 2009;22:919–926.